4-2024

Inertial Particle Clustering due to turbulence in an air jet

Bianca Viggiano
Portland State University, viggiano@pdx.edu

Kris Gish
Washington State University Vancouver

Stephen Solovitz
Washington State University Vancouver

Raul Bayoan Cal
Portland State University, rcal@pdx.edu

Citation Details

Viggiano, B., Gish, K., Solovitz, S., & Cal, R. B. (2024). Inertial particle clustering due to turbulence in an air jet. International Journal of Multiphase Flow, 174, 104734.

Inertial particle clustering due to turbulence in an air jet

Bianca Viggiano [a,b,*], Kris Gish [c], Stephen Solovitz [c], Raúl Bayoán Cal [b]

[a] *Department of Mechanical Engineering, Polytechnique Montréal, Montréal, QC H3C 3A7, Canada*
[b] *Department of Mechanical and Materials Engineering, Portland State University, Portland, OR 97207, USA*
[c] *School of Engineering and Computer Science, Washington State University Vancouver, Vancouver, WA 98686, USA*

ARTICLE INFO

ABSTRACT

Explosive volcanic eruptions create turbulent plumes of fine ash particles. When these particles collide in the presence of moisture and electrostatic fields they combine into larger aggregates, which can significantly change the atmospheric residence time of the airborne cloud. Previous studies have suggested that turbulence may lead to preferential concentration—also known as clustering—of particles within the flow, increasing the likelihood of collisions and aggregation. Few experimental studies have quantified these processes for volcanic plumes. This behavior was investigated using a particle-laden air jet. By systematically varying the exit speed and the size, density, and concentration of particles, flows were produced with Reynolds numbers of 4940 to 19300, Stokes numbers of 1.0 to 17.4 (based on the convective scale), and particle mass loadings of 0.3 to 3.9%. Specific emphasis is placed on two Stokes numbers of 1.9 and 17.4, which differ by nearly an order of magnitude. Particle image velocimetry was employed to measure the velocity distribution within a two-dimensional rectangular region along the jet centerline in each experiment. Voronoï decomposition was used to quantify the extent of preferential concentration by measuring the distribution of cell sizes around each individual particle. Results show that particles exhibit clustering behavior when Stokes numbers are close to 1. We also measured the radial distribution functions (RDFs) to quantify the likelihood of particle collisions. At low Stokes number, the RDF magnitude was significantly higher, which corresponds to increased collision frequency in the particle-laden jet. Computational analysis finds that increasing the RDF by a factor of 20 results in a doubling of peak aggregate size. These findings demonstrate that preferential concentration due to turbulent structures could have important effects on collision frequencies, ash aggregation, and electrification in volcanic plumes.

1. Introduction

Large explosive volcanic eruptions can propel significant quantities of fine-grained volcanic ash (<63 μm) into the upper atmosphere. Individually, these ash particles settle very slowly, traveling hundreds to thousands of kilometers before falling back to the surface of the Earth. However, it is commonly observed that fine particles stick together and form larger aggregates, which dramatically changes their effective diameter and, therefore, their atmospheric residence time. For example, during an explosive event from Alaska's Redoubt Volcano in 2009, >95% of fine ash in the deposit landed as aggregates (Van Eaton et al., 2015). Volcanic ash can be hazardous, impacting aircraft engines, water supplies, and respiration (Dunn, 2012; Wilson et al., 2015). Because of these concerns, it is important to understand the aggregation process to develop better forecasts of ash transport and deposition. Specifically, we need to consider the influence of particle behavior on the large-scale mechanics.

The key physical mechanisms of ash aggregation are well established. Some of the early observations of the May 18, 1980 eruption of Mount St. Helens, Washington, showed that ash aggregates could be held together by electrostatic attraction (Sorem, 1982), and laboratory experiments with a powder-coating device reproduced this behavior (Schumacher, 1994). Aggregates also combine in the presence of moisture (Tomita et al., 1985), particularly near or at water saturation, as demonstrated through vertical wind tunnel (Gilbert and Lane, 1994) and atmospheric chamber experiments (Telling et al., 2013). Turbulence plays a role in aggregation by increasing the chance for particle collisions, although it has been suggested that its impact is minor compared to differential settling of a wide range of particle sizes (Costa et al., 2010). Recent studies into cohesion-induced particle agglomeration have been carried out experimentally and numerically by Zhang et al. (2023) and Chen et al. (2019), respectively. However, there have been few experimental studies focused on the impacts of turbulence on particle-laden flow behavior and aggregation. Moreover,

---

* Corresponding author at: Department of Mechanical Engineering, Polytechnique Montréal, Montréal, QC H3C 3A7, Canada.
E-mail addresses: bianca.viggiano@polymtl.ca (B. Viggiano), kris.gish@wsu.edu (K. Gish), stevesol@wsu.edu (S. Solovitz), rcal@pdx.edu (R.B. Cal).

there is limited quantitative data on these mechanisms for scales and geometries pertinent to volcanic eruptions, which presents a challenge for developing appropriate fallout models.

Over the past decade, some ash dispersal models have begun incorporating aggregation processes (Costa et al., 2010; Folch et al., 2010; Beckett et al., 2022; Hoffman et al., 2023). They use the classic Smoluchowski model, which tracks the number of particles of a particular size over time (Smoluchowski, 1918). This method requires two inputs to determine the rate of aggregation — the frequency of particle collision and the efficiency of sticking between them. Collision frequency depends on a variety of properties, including particle size, relative speed, and their distribution within the flow, which can be estimated using classic models of randomly distributed particles (Saffman and Turner, 1956). Sticking efficiency is more complex to evaluate, but empirically based forms have been determined based on experimental data (Gilbert and Lane, 1994; Egan et al., 2020) including more recent, high-humidity experiments (Hoffman and Eaton, 2023). For example, the revised plume model of Hoffman et al. (2023) used experimental data to develop its aggregation module, but the effects of turbulence were heavily parameterized. In natural eruptions, particles are not evenly or randomly distributed throughout the flow; variations in flow structure and turbulence create regions of preferential concentration. Particles collect within regions of low vorticity (Eaton and Fessler, 1994), particularly when their inertial response is not long in comparison to time scales of the fluid. This local increase in concentration leads to a local increase in collisions frequency (Sundaram and Collins, 1997), which has a direct influence on aggregation rates.

Most studies of preferential concentration have focused on canonical flows, such as homogeneous isotropic turbulence (Squires and Eaton, 1990; Elgobashi and Truesdell, 1992; Reade and Collins, 2000; Holtzer and Collins, 2016; Chen et al., 2006), homogeneous shear (Gualtieri et al., 2013), and channels (Kulick et al., 1994; Esmaily et al., 2020). For jet flows, this phenomenon was studied by Longmire and Eaton (1992). Using flow visualization and laser Doppler anemometry, they examined fluid and particle behavior with a jet with periodic forcing. Dense particle clusters collected in the jet shear layer, localized in the high-strain regions between vortices. Clustering persisted over a wide range of particle loadings, even at more than 50% of the total mass in the flow. Similar clustering was observed by Wicker and Eaton (2001) for a more complex, swirling jet. Birzer et al. (2011) applied a planar nephelometry technique to identify large-scale features in a coaxial jet, demonstrating that instantaneous particle distributions differ strongly from the mean. For a similar geometry, Lau and Nathan (2017) subsequently developed an automated technique to identify clusters, observing long, narrow bands within the flow even near the jet exit. These particular structures were later determined to stem from the turbulent boundary layer of the long pipe upstream of the exit (Lau et al., 2019). Capone et al. (2023) studied the effects of particle-to-fluid density ratios on preferential concentration in the near field of a particle-laden jet. For low Stokes number flows, they found that low particle-to-fluid density ratios lead to particles migrating near the centerline. Higher density ratios lead to migration of particles toward the jet pipe walls. These trends tend to vanish as the jet develops farther downstream.

In each of these studies, clustering was strongly connected to the Stokes number of the flow. Stokes number is a ratio of timescales, $St = \tau_p/\tau_{flow}$, relating the particle aerodynamic response to the governing flow conditions. For low Reynolds numbers, the particle time scale is $\tau_p = \rho_p D_p^2/(18\mu)$ based on Stokes flow, where ρ_p, D_p, and μ are the particle density, particle diameter, and fluid viscosity, respectively. Several values have been used for the flow time scale, τ_{flow}, though common choices include the Kolmogorov scale for turbulence (Balachandar and Eaton, 2010) and the convective timescale, D/U_J (Lau and Nathan, 2017). Here, D and U_J are the jet exit diameter and speed, respectively. For $St \ll 1$, particles have negligible inertia, so they follow the flow faithfully without clustering. For $St \gg 1$, particles have enough inertia

that they do not respond rapidly to the flow, maintaining their earlier velocities and distribution for significant distances. However, when the Stokes number is near one, particles tend to cluster in high-strain regions.

Several methods have been used to quantitatively analyze preferential concentration (Monchaux et al., 2012). Perhaps the most common technique employs a clustering index (Fessler et al., 1994), which typically involves subdividing an image of the flow into an array of boxes. The index compares the number of particles in each box to a random particle distribution. Although this method can help identify typical cluster scales, it shows sensitivity to the box size and the total number of particles (Banko, 2018). Fortunately, other clustering metrics can avoid these challenges.

Voronoï diagrams help to identify areas of preferential concentration while avoiding the arbitrary selection of a length scale (Monchaux et al., 2010; Obligado et al., 2014; Baker et al., 2017). This method has utility in the examination of turbulent flows, such as numerical and experimental homogeneous turbulence (Tagawa et al., 2012) and numerical channel flow in a variety of configurations (Nilsen et al., 2013). In this technique, an image is divided into cells surrounding each individual particle, with boundaries defined so that each point in the sub-region is closer to that particle than any other. Cell sizes, shapes and distributions may be linked to the cluster density, and scaling permits study of their fractal dimension. This latter parameter may be beneficial for study of ash aggregation, as the cluster structure can impact the growth rate.

The radial distribution function (RDF) provides a metric that is independent of the number of particles. The RDF, $g(r)$, determines the probability of finding a particle located at a distance r relative to a random distribution (Gualtieri et al., 2013; Larsen and Shaw, 2018). If there is preferential concentration, the RDF exceeds a value of one, indicating a greater likelihood of collisions between particles. Practically, this has a direct connection to ash aggregation processes since the collision frequency increases the rate of aggregation if moisture or electrostatic fields are present.

Voronoï decomposition and RDF analysis have been used for a variety of geometries, but there has been limited application to jet flows, particularly at scales appropriate for volcanic eruptions. To our knowledge, only one study has used Voronoï decomposition in jet flow, and focused solely on the flow at the exit (Lau et al., 2019).

In this analysis, a particle-laden jet is used to examine conditions that pertain to volcanic eruption plumes. Using a well-characterized air jet within a large laboratory, the presence or absence of preferential concentration over a range of Reynolds numbers, Stokes numbers, and particle mass loadings is quantified. The effect of clustering on ash aggregation is demonstrated through a computational model. The overall goal is to consider how these small-scale physical mechanisms may impact large-scale processes in airborne volcanic plumes.

2. Experimental methods

2.1. Apparatus

The jet experiments were performed at Washington State University –Vancouver, using a rigid pipe apparatus that generates a vertical upward jet. These experiments have been described in detail in Shannon et al. (2023). As depicted in Fig. 1, regulated, compressed air is fed into the system, where it is directed into a fluidized bed for particle seeding. The two-phase mixture of air and particles exits the bed through a narrow horizontal pipe, which helps draw particles into the flow via a Venturi effect. The flow then feeds into a vertical pipe with an inner diameter of 15.8 mm, which tapers to 6.83 mm through a fifth-degree polynomial nozzle (Bell and Mehta, 1988). After this contraction, the pipe diameter remains constant for 15.2 cm prior to ejection into the laboratory area through a horizontal baseplate. This setup provides sufficient non-dimensional length for fully developed, turbulent exit
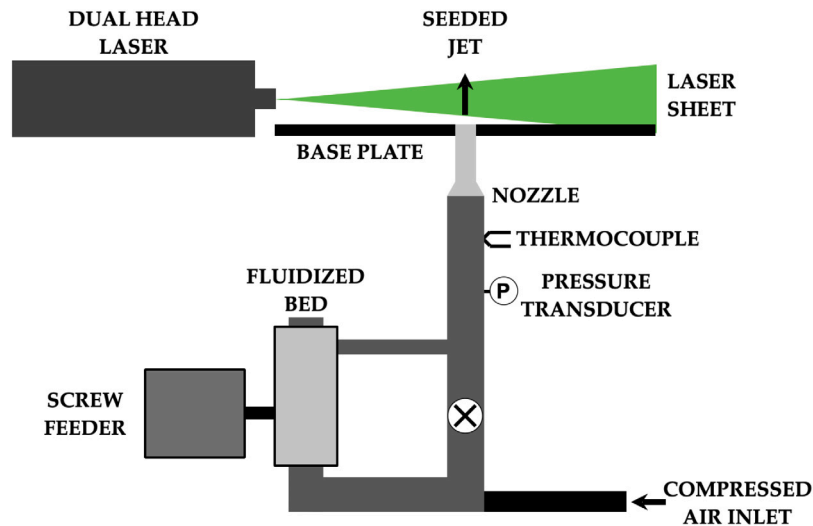
Fig. 1. Schematic of experimental apparatus to produce a turbulent, particle-laden air jet.
Source: Adapted from Solovitz et al. (2011).

conditions (Kays and Crawford, 1993). The system has been adapted from a previous test fixture (Solovitz et al., 2011; Viggiano et al., 2021b), and previous measurements have demonstrated that the unladen velocity profile is logarithmic at the exit, as expected (Saffaraval and Solovitz, 2012).

Exiting flow is monitored for consistency using a gauge pressure transducer and T-type thermocouple. An additional pressure transducer is also located upstream of the inlet of the system. The apparatus is placed within a large enclosure to isolate the experiments from ambient flow variation in the laboratory. This rectangular prismatic structure has a cross-section of 2.44 m by 2.44 m and a height of 3.66 m, and it features flexible plastic walls. The dimensions were selected to mitigate recirculation within the enclosure (Hussein et al., 1994), with a momentum change of less than 1%.

2.2. Particle seeding

Solid particles are injected by a commercial screw feeder at a constant mass flow rate. The feeder output is adjustable, with a calibrated resolution of $\pm2\%$. For a given jet speed, the output mass flow is chosen to produce a desired mass loading. To account for any particle loss prior to the jet exit, the total mass injection is also measured directly using a high-accuracy scale (±1 g out of a 8.2 kg range). Before and after each experiment, both the screw feeder and the fluidized bed were weighed. In addition, the rest of the pipe apparatus was thoroughly vacuumed after each experiment, and the vacuum bag was also weighed to determine the quantity that did not reach the exit. The total mass injection was calculated using the difference between the measurements before and after each test. Two types of spherical particles were injected for these experiments — solid nickel and hollow glass. Each particle has approximately the same diameter, D_p, of 14 μm for nickel and 13 μm for hollow glass, as verified with a laser diffraction particle size analyzer. However, the respective particle densities are significantly different, measured at 8900 kg/m^3 for nickel and 1100 kg/m^3 for hollow glass. This leads to a wide range of Stokes numbers while maintaining nearly identical jet Reynolds numbers. More discussion of the particle seeding process is given by Shannon et al. (2023).

2.3. Particle imaging

Particles are imaged with a commercial particle image velocimetry (PIV) system, which uses a 4-megapixel charge-coupled device

(CCD) camera and a dual-head, frequency-doubled Nd:YAG laser. Optics produce a laser sheet of approximately 0.5 mm thickness, which illuminates an 8.5 cm by 17 cm region passing through the jet centerline. The system synchronizer rapidly triggers both the camera and laser twice, which captures the successive positions of particles within the flow. The delay time between images is on the order of 20 μs, which is sufficient to depict the particle motion.

Image pairs are processed using Pivlab2000 (Han, 2001), which determines the local instantaneous velocity field. The images are divided into interrogation regions, which are cross-correlated to find the particle displacement using a Gaussian fit for the peak. The software uses seven processing passes, starting with interrogation regions of 128 by 128 pixels and gradually progressing down to 32 by 32 pixels. This results in a final vector spacing of 1.1 mm when using a 50% overlap. The velocity uncertainty is estimated at $\pm1.3\%$ through a propagation of uncertainty analysis, which considered the accuracy of the post-processing scheme (Raffel et al., 2013), the camera calibration factor, and the synchronizer timing. For each test condition, a total of 1000 image pairs was captured, which is sufficient for convergence of low-order turbulent velocity statistics.

For analysis in this study, particle tracking is employed on the nickel and hollow glass spheres. The particles are detected using a series of classical image processing methods (Viggiano et al., 2021a; Basset et al., 2022). First, the images are corrected for nonuniform illumination. For each raw camera image, the particles are at high intensity and the background at low intensity. Second, the image is modified morphologically, generating an opening through an erosion technique followed directly by a dilation process using a 3 to 5 pixel diameter disk. This step keeps only the particles within the image while setting the background to zero, thus removing noise from the input. Third, the modified image is thresholded, which removes low intensity points to eliminate defects smaller than the particle of interest. Finally, the image is locally binarized to detect the centroids of the particles using standard functions for region analysis within Matlab. These particle centers serve as the input for calculation of the Voronoï regions and the radial distribution functions. Fig. 2 shows sample results from this particle detection process, displaying individual images for both hollow glass and solid nickel particles. The size of the two jets varies significantly, which qualitatively indicates the influence of the particles on the spreading rate. We note that some particles linger in the ambient after the initial runs of the experiment, observed in the outer regions of the interrogation area. Furthermore, particles appear to be absent from the bottom and top of the images due to the location of the laser sheet.
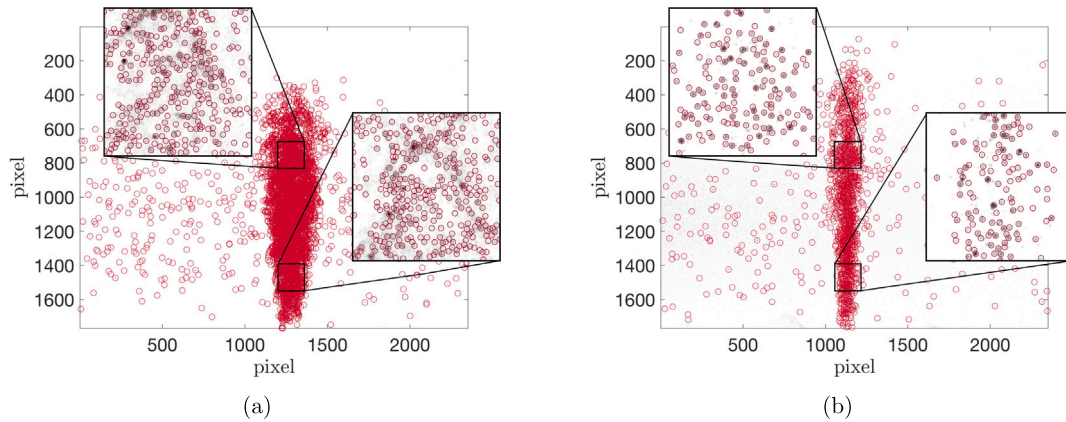
Fig. 2. Representative images of particle detection results using (a) hollow glass and (b) nickel particles. The insets display zoomed images within the jet.

Table 1

Experimental parameters of the considered cases where Re_D and St are the Reynolds number and the Stokes number, defined in the text. U_J is the jet exit velocity, and Φ is the mass loading of the particles. All test cases are previously discussed by Shannon et al. (2023).

Test case	Particle type	U_J [m/s]	Re_D	St	Φ
$Ni_{Re-5,St-9}$	Nickel (14 μm)	11.4	4940	9.0	3.6%
$Ni_{Re-10,St-17}$		22.1	9600	17.4	3.9%
$HG_{Re-5,St-1}$	Hollow glass (13 μm)	11.4	4940	1.0	1.5%
$HG_{Re-10,St-2,\Phi-0}$		22.1	9600	1.9	0.3%
$HG_{Re-10,St-2,\Phi-1}$					1.3%
$HG_{Re-10,St-2,\Phi-2}$					2.0%
$HG_{Re-20,St-4}$		44.3	19 300	3.7	1.2%

2.4. Test conditions

Using the experimental setup shown in Fig. 1, Shannon et al. (2023) analyzed eighteen different flow configurations by varying the jet speed, particle type, and particle mass flow. The scaling of these experiments compare reasonably well with natural volcanic plumes, and best represent the near-vent exit region (Shannon et al., 2023). For this study, we selected seven of these experimental tests for more detailed analysis. Table 1 provides the test conditions, along with the associated non-dimensional parameters, including the Reynolds number with respect to exit jet diameter, $Re_D = \rho_f U_J D/\mu$, the Stokes number based on the convective time scale (defined earlier), and the mass loading of the particles, $\Phi = \dot{m}_p/\dot{m}_f$. Here, ρ_f, U_J, D, $\dot{m}_p$, and $\dot{m}_f$ are the exit fluid density, jet velocity, jet diameter, particle mass flow rate, and fluid mass flow rate, respectively. We note here that the Stokes number based on the standard convective time scale is chosen due to its direct link with the eddy turnover time, which corresponds to the most energetic scales. More details on this can be found in Shannon et al. (2023).

These test cases were selected to consider conditions relevant to volcanic eruptions, as detailed in the scaling analysis by Shannon et al. (2023). Natural eruptions have much larger Reynolds numbers (Sparks et al., 1997), ranging from $\sim 10^3$ to $\sim 10^9$. Our experiments consider the lower portion of this range, from $\sim 5 \times 10^3$ to $\sim 2 \times 10^4$, but still within the fully turbulent regime. Within an eruption, Stokes numbers can range from $\ll 1$ to $\gg 1$. Near the exit, we expect $St > 1$ due to relatively large exit speeds and particle sizes. At other locations, particles can have $St \sim 1$. Typically, this condition corresponds to particle diameters from hundredths of a millimeter to a few millimeters, depending on the location and the fluid time scale. We consider conditions from 1.0 to nearly 20, where preferential concentration is likely. Again, the Stokes

number is defined here using the convective time scale of the fluid, which is often used for particle laden jets (Lau and Nathan, 2017). Finally, volcanic plumes may have significant particle mass loadings, particularly near the exit, where the magnitude may exceed 90%. As the plume rises, the mixture is diluted due to air entrainment and particle fallout, reducing the loading to $\sim 5\%$ at a few kilometers above the exit (Mastin, 2007). These experiments examine loadings relevant to these higher elevations, from 0.3% to $\sim 4\%$. Some preliminary tests were conducted at higher loading, but the images were too saturated to display clear particle clustering.

3. Analytical techniques

3.1. Voronoï distribution

Voronoï tessellation analysis is a widely used method to quantify spatial distributions of a set of points. In general, this method results in a set of cells that surround each particle within the image. The cell boundary includes only the region which is closer to the given particle than any other particle. With preferential concentration, there is a greater likelihood that cells will be very large (voids) and very small (clusters).

Edelsbrunner and Seidel (1986) provide a general method for the mapping of any domain by using a set of functions. Mathematically, Voronoï mapping takes a set of sites (particle points in space) and transforms them into partitioned regions. For a given 2D domain in space, Ω, there are n sites present within the plane. The ending location of the cell is found by defining two distinct sites, $\alpha, \beta \in \Omega$, and determining the dominance of one site over another. This is defined as:

$$\text{dom}(\alpha, \beta) = \left\{ x \in R^2 \mid \delta(x, \alpha) \leq \delta(x, \beta) \right\}, \tag{1}$$

where δ is the Euclidean distance function. The dominance is a half plane bounded by the bisector of α and β, separating all points closer to α from those closer to β. This can be repeated to form a region of a site:

$$\text{reg}(\alpha) = \bigcap_{\beta \in \Omega - \{\alpha\}} \text{dom}(\alpha, \beta), \tag{2}$$

where the corresponding portion of the domain contains all of the dominances of α over remaining sites in Ω. This technique is easily applied via algorithms available in analytical software, such as Matlab.

In application of the Voronoï method on 2D images of a 3D flow some biases may exist, such as overlapping of particles and out-of-plane distance approximations (Banko, 2018). These can be mitigated through low levels of mass loading and ensuring a thin laser sheet thickness, respectively, which have been employed in this study.
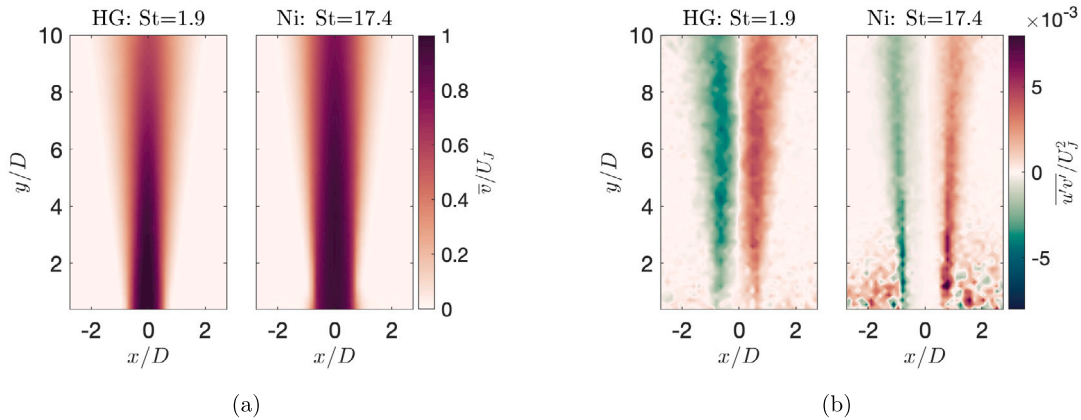
Fig. 3. Contours of (a) mean axial velocity and (b) cross-correlation between transverse and axial fluctuations for the hollow glass (HG) particles at $\Phi = 2.0\%$ and the nickel (Ni) particles at $\Phi = 3.9\%$. The x and y locations are normalized by the jet diameter D. Both cases consider $Re_D = 9600$. The increased diffusion of the HG-laden jet in comparison to the Ni-laden jet is observed in both the mean and shear stress contours.

3.2. Radial distribution function

The radial distribution function provides a quantitative metric that indicates the proximity of particles compared with a random distribution. This method results in a function, $g(r)$, that exceeds one when particles are clustered. Conceptually, the RDF derives from the pair correlation function, as described by Landau and Lifshitz (1980). Two small, separate volumes, dV_1 and dV_2, have centers located a distance r apart. If the overall domain has a mean number density, $\bar{n} = N/V$, then the probability that both volumes contain a particle is:

$$p_{12}(r) = (\bar{n}dV_1)(\bar{n}dV_2)g(r), \qquad (3)$$

where N is the number of particles, V is the domain volume, and $g(r)$ is the RDF. For a random distribution, $g(r) = 1$ at all r. If $g(r) > 1$, then there is an increased probability of locating particles at this distance.

When particle locations are known, the RDF may be computed using a ratio between the measured number of particles and the expected number from a random Poisson distribution (Larsen and Shaw, 2018). Mathematically, this has the form:

$$g(r_j) = \sum_{i=1}^{N} \frac{\psi_i(r_j)/N}{(N-1)(dV_{r_{i,j}}/V)}, \qquad (4)$$

where $\psi_i(r_j)$ is the number of particles with a center at a radial distance between $r_j - \delta r_j$ and $r_j + \delta r_j$ from particle i. Here, $dV_{r_{i,j}}$, is the shell volume between radial distances $r_j - \delta r_j$ and $r_j + \delta r_j$, N is the total number of particles, and V is the total measured volume.

In practice, the computed RDF can be biased due to practical challenges with experimental imaging. First, at very small distances, particles cannot be distinguished as separate entities, so $g(r)$ decreases to zero even when clustered. Second, for 2D images of a 3D domain, particles may also appear to overlap due to their projection onto a plane, attenuating the 2D form of the RDF. However, correction factors (Holtzer and Collins, 2002) may be implemented to recover the magnitude of $g(r)$ to within 10%. Third, as distances approach the domain size, the shell volumes may extend beyond the image boundary, resulting in inaccurate particle counts. Larsen and Shaw (2018) demonstrate that the RDF may still be evaluated accurately when considering only the portion of the shell volume contained within the image domain.

4. Results

4.1. First and second-order statistics

First, we present overall flow statistics of the particle dynamics, obtained from the PIV measurements, which display the influence of particle inertia. Fig. 3(a) shows the time-averaged axial velocities $\bar{v}$ at two different Stokes numbers, while Fig. 3(b) provides the corresponding cross-correlations between the transverse and axial velocity fluctuations, u' and v', respectively. The two cases have the same Reynolds number of 9600 and similar mass loading near 3%. However, the Stokes numbers in these cases differ by nearly an order of magnitude, at 1.9 with hollow glass and 17.4 with solid nickel. The mean velocities are normalized by the jet exit velocity, U_J, while the transverse (x) and axial (y) locations are normalized by the nozzle diameter, D. The cross-correlations are normalized by the jet exit velocity squared, U_J^2. For a single-phase flow, these first and second-order statistics would represent the mean velocity and the Reynolds shear stress, respectively. In these measurements, though, the focus is on the particle motion, which differs from the air carrier fluid due to the increased particle inertia. Since the concern is on particle clustering and eventual aggregation, the particle motion is more critical here.

In Fig. 3(a), the mean particle velocity for the hollow glass displays a short jet core, which rapidly diffuses out and decreases in speed relative to the nickel case. The higher density nickel particles contain greater inertia, increasing the core size and decreasing the streamwise decay of the axial velocity. In Fig. 3(b), the cross-correlation of the hollow glass particles has greater magnitude and radial extent when compared to that of the nickel particles. At the higher Stokes number, the magnitude is significant only along the edges of the jet, retaining similar levels throughout the measurement domain. Because of the high particle inertia within the core, there is less responsiveness to turbulent fluctuations within the carrier fluid very near the exit nozzle of the jet, and particle velocity fluctuations are much reduced within the jet. Although some effects are observed in both cases here, this inertia is felt more by the heavier nickel particles. This is evident from the larger core, corresponding to low cross-correlations in Fig. 3(b). Although only two test cases are shown here, these trends are consistent over all experiments, as quantitatively validated by Shannon et al. (2023).

4.2. Voronoï decomposition

Next, the clustering of particles is examined through Voronoï decomposition. Each experimental image is decomposed into individual cells, each containing a single particle. By definition, the area of the Voronoï cell is the inverse of the particle concentration. Therefore, the distribution of tessellation areas provides a direct metric for the concentration field. For randomly distributed particles, the cell areas should follow a Poisson distribution, and any deviations from this form represent clustering effects (Monchaux et al., 2010).

The cell distribution is compared for the same two cases as Fig. 3. These have the same Reynolds number and similar mass loading but
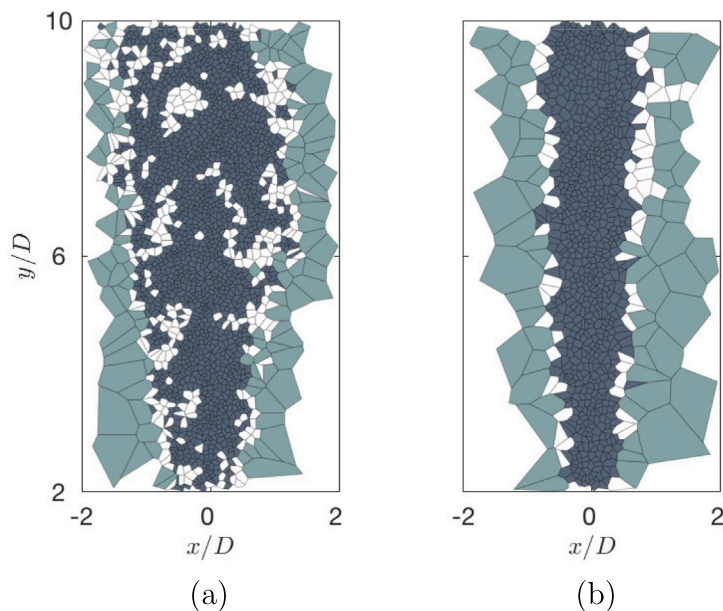
Fig. 4. Voronoï tessellations for an arbitrary individual snapshot with (a) hollow glass spheres and (b) nickel particles. Clusters and voids are signified by dark and light gray shading, respectively. For both cases, $Re_D = 9600$ and $\Phi \sim 3\%$.

different Stokes numbers. Individual snapshots of the decomposition qualitatively show the clustering behavior. Fig. 4 displays the Voronoï mapping of the "clusters" and "voids" for individual snapshots with hollow glass and nickel particles. (These terms are formally defined using probability density functions later.) Clusters and voids are shaded differently, shown in dark gray and light gray, respectively. The nickel particles have uniform clustering along the core of the jet, with voids occurring within the outer regions of the ambient at $|x|/D \gtrsim 1$. In contrast, the hollow glass spheres have very small cells within the core of the jet, with clusters formed at different regions. There are larger voids surrounding the jet as the flow transitions into the quiescent ambient fluid. The clusters show denser structures occurring on each side of the jet, spaced ~ 1 to 2 diameters apart. This is comparable to the distance between shear layer vortices along the jet boundary, which have been shown to generate particle clustering (Longmire and Eaton, 1992). This suggests that these lower inertia particles are following the flow better than the heavier nickel particles.

This figure provides a schematic to better understand the types of clustering that occur in the two particle-laden jets. Although clustering is prevalent in both the HG and Ni-seeded jets, the distribution of the clusters varies significantly. These characteristics of clustering and non-clustering regions of the jet are easily visualized in the schematic. The quantitative behavior of cluster form and propagation are further quantified by probability density functions (PDFs) of the cell areas and RDFs later. Fig. 5(a) displays the PDFs for the cell areas at $Re_D = 9600$ and $\Phi \sim 3\%$ for hollow glass spheres ($St = 1.9$) and nickel particles ($St = 17.4$). The cell areas are normalized by the mean local area, using $\nu = \mathcal{A}/\mathcal{A}_{mean}(x, y)$, which accounts for the inhomogeneity of the jet (Sumbekova et al., 2017). This ensures that the true clustering based on the particles within the geometry is accurately captured, mitigating the spatially nonhomogeneous flow field effects. This technique does differ from the more classical normalization methods for quantifying clustering through cell area PDFs and therefore discrepancies in the locally normalized PDFs could arise (Monchaux et al., 2012; Baker et al., 2017). A random Poisson distribution (RPP) is also included (Ferenc and Néda, 2007), which helps provide classifications between clusters and voids.

In Fig. 5(a), both measured PDFs show similar trends, although the tails extend to more extreme sizes at $St = 1.9$. This demonstrates that both smaller areas and larger areas are more likely at this condition. Increased clustering produces more dense particle concentration, resulting in smaller cell areas. More voids would similarly produce larger cell areas. This suggests that clustering is increased when the Stokes number is near unity. This coincides with lower-density particles (hollow glass), where concentrations occur in high vorticity regions. For higher inertia cases, the particles do not respond well to flow variation, so they maintain their original, narrower distribution farther downstream.

Additional structures are defined using the points where the PDFs cross the Poisson distribution. For each case, there are three crossings — two on the right of the PDF peak, and one on the left. The two crossings on the right are the focus here. Cells larger than the rightmost crossing are termed "voids", as they represent large areas with more distant neighboring particles. Cells smaller than the other crossing on the right are termed "clusters", since they have small areas with closer neighbors. The crossing on the left is not used because it only corresponds to a very limited total number of cells.

The effects of Reynolds number are considered by examining the clustering behavior for a specific particle type and mass loading. Fig. 5(b) shows the PDFs for the Voronoï cell area with hollow glass spheres at three different Reynolds numbers. In each case, a similar mass loading near 1.3% is used. Technically, the Stokes number also changes with Reynolds number due to the velocity dependence, but the range (from $St \sim 1$ to 4) is significantly below the levels for the solid nickel particles. All PDFs show an overlap for modest Voronoï cell sizes in the middle of the distribution, with differences seen mostly in the tails on either end. With increasing Reynolds number, the PDF narrows, with lower probability densities at the extrema. This indicates a reduction in the number of small clusters and large voids, resulting in more consistent particle spacing. Still, the three cases overlap over most of the PDF, notably within the transitional region between clusters and voids. This overlap has also been observed in channel flow experiments (Banko, 2018). When examining the crossing points with the Poisson distribution, there is an increase in the normalized area as a function of decreasing Reynolds number for the clustering as well as the voids.

The importance of mass loading is considered by examining a consistent particle type and Reynolds number. Fig. 5(c) displays PDFs of normalized Voronoï cell area considering hollow glass spheres at
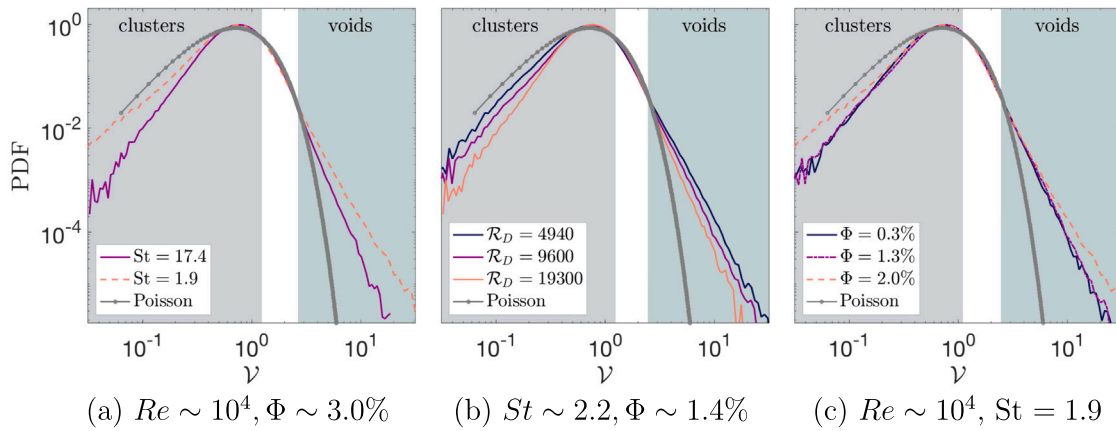
(a) $Re \sim 10^4, \Phi \sim 3.0\%$ (b) $St \sim 2.2, \Phi \sim 1.4\%$ (c) $Re \sim 10^4, St = 1.9$

Fig. 5. Probability distribution functions of the locally normalized Voronoï area, $\mathcal{A}/\mathcal{A}_{mean}(x, y)$, for (a) varying Stokes number, (b) varying Reynolds number and (c) varying mass loading. For all cases, the Poisson distribution is shown for comparison, and the clusters and voids are distinguished by examining where the PDFs cross the Poisson distribution.
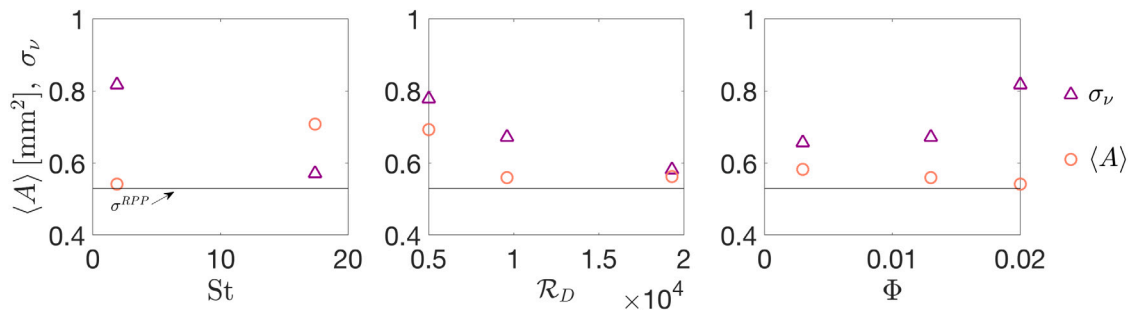

Fig. 6. Average cell area, $\langle A \rangle$ (in mm^2), and standard deviation of the normalized area, σ_ν, for each considered case. The three comparisons consider varying Stokes number ($Re_D = 9600$ and $\Phi \sim 3\%$), varying Reynolds number (Hollow glass with $\Phi \sim 1.3\%$), and varying mass loading (Hollow glass with $Re_D = 9600$). The RPP standard deviation is also indicated.

$Re_D = 9600$, which corresponds to $St = 1.9$. Although the range of mass loadings is relatively small (0.3% to 2.0%), there is still a significant variation ($\sim$7X) in number density. Examining the distributions, there is some dependence on the loading of the particles. This is evident in the tails of the PDFs, as the lower and intermediate loadings of 0.3% and 1.3% show lower probability compared to the higher mass loading case. However, the tails only consider a relatively small number of cells, and the deviation is modest. Overall, the differences over the entirety of the curves are small in comparison to the effects due to Stokes number and Reynolds number in Fig. 5(a) and (b), respectively, indicating the mass loading has a minor impact on clustering behavior.

In all cases, most changes occur near the tails of the distribution, which represent the largest clusters and voids. Even so, the PDFs in Fig. 5(a), (b), and (c) show only modest deviations when changing St, Re_D, and Φ, respectively. All of the cases are clearly different from the random Poisson distribution, though, which is reasonable because the underlying jet flow structure has a non-homogeneous structure.

We further quantify the clustering behavior through the average cell area and its standard deviation, as presented in Fig. 6 and Table 2. We also include the lowest and highest points where the PDFs cross the Poisson distribution. The average cell area directly corresponds to particle concentration. The standard deviation provides a quantitative metric for the amount of clustering, as deviation from the RPP indicates the presence of clustering within the field (Monchaux et al., 2010). The three comparisons in the figure consider the effects of Stokes number, Reynolds number, and mass loading. First, a clear Stokes number dependence is seen in Fig. 6(a). Comparing $St = 1.9$ and 17.4, the standard deviation of the cell area is significantly larger when the Stokes number is closer to one, indicating a larger range of cell sizes. This occurs even though the two cases have similar cell area size on average (0.49 mm^2 and 0.63 mm^2). Second, the average

cell area displays a natural Reynolds number dependence in Fig. 6(b), showing a decrease in size at higher Re_D. This occurs because higher jet speeds result in an increased fluid mass flow rate, requiring higher particle concentration to maintain the same mass loading. Note that the tessellation statistics are solely dependent on the dispersed phase dynamics, and different trends maybe be observed in the carrier phase, as suggested in Sumbekova et al. (2017). The standard deviation also shows a decreasing trend with Re_D. Third, a reasonable mass loading dependence is found in Fig. 6(c), again showing a gradual decrease in average cell areas with increasing Φ. For a given Reynolds number, a higher loading requires more particles and reduced particle spacing. In addition, there is some increase in the standard deviation with higher mass loading.

Table 2 also provides comparisons of the cell area and standard deviation for these cases. The data are presented in terms of increasing parameter values, organized by Reynolds number, Stokes number, and finally mass loading. When the standard deviation of the normalized area (σ_ν) of the particles exceeds that of a RPP ($\sigma_\nu^{RPP} = 0.53$), clustering occurs. All of the test cases have σ_ν greater than σ_ν^{RPP}, which indicates some clustering at every condition. However, the effect is relatively small in the nickel-laden flow and in the highest Reynolds number case.

4.3. Radial distribution functions

Next, the radial distribution function is used to quantitatively examine the clustering behavior, which provides a metric related to the collision frequency. Figs. 7 to 9 display the RDFs, $g(r)$, for various regions, considering different Stokes numbers (1.9 and 17.4) at the same Reynolds number (9600) and mass loading ($\sim$3%). These test conditions are identical to Figs. 3, 4, and 5(a). The radial position, r, is normalized by particle diameter, representing the number of diameters

Table 2
Average cell area, $\langle A \rangle$ (in mm^2), standard deviation, σ_v, and Voronoï crossings for each test case.

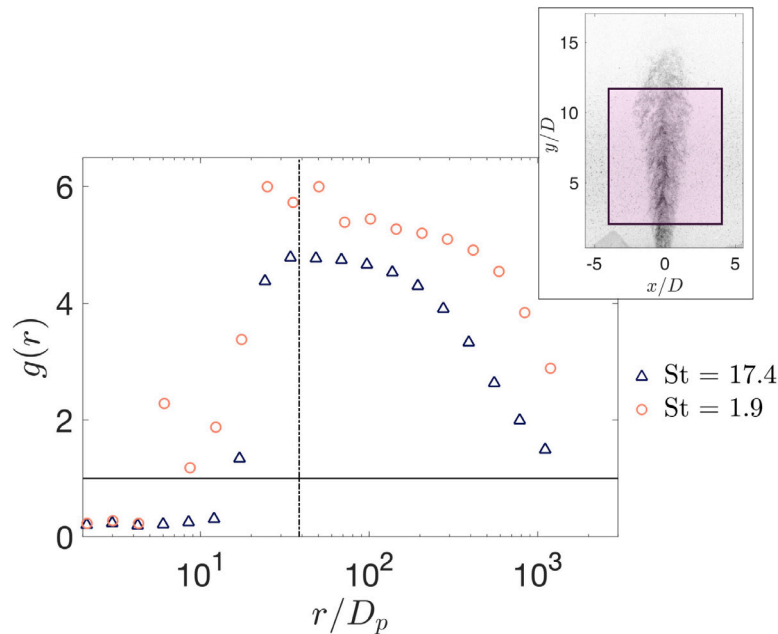| Re_D	St	Φ	$\langle A \rangle$ [mm^2]	σ_v	Voronoï crossing (low)	Voronoï crossing (high)
4940	1.0	1.5%	0.69	0.78	1.05	2.48
9600	1.9	0.3%	0.58	0.66	1.15	2.49
9600	1.9	1.3%	0.56	0.67	1.20	2.64
9600	1.9	2.0%	0.54	0.86	1.10	2.61
9600	17.4	3.9%	0.71	0.57	1.28	2.74
19 300	3.7	1.2%	0.56	0.58	1.30	2.74

Fig. 7. Radial distribution functions, $g(r)$, for hollow glass spheres ($St = 1.9$) and nickel particles ($St = 17.4$) over the streamwise domain of $2 \leq y/D \leq 12$, and a transverse range, $-4 \leq x/D \leq 4$. All cases consider $Re_D = 9600$ and $\Phi \sim 3\%$. The radial coordinate, r, is normalized by the particle diameter, which is nearly the same for both particle types The laser sheet position is demarcated with a vertical dash dot line.

between particles. The RDFs are evaluated in three different regions to better understand the downstream development of clustering. First, the majority of the jet is included in our region of interest, shown in Fig. 7. This extends over an axial range, $2 \leq y/D \leq 12$, and a transverse range, $-4 \leq x/D \leq 4$, which includes the jet core and ambient as the flow develops. Second, we study the near-exit region in Fig. 8, which only extends over an axial range from $2 \leq y/D \leq 6$. Third, we consider a fully developed region for the mean flow in Fig. 9, extending from $8 \leq y/D \leq 12$.

Over the entire jet region (Fig. 7), both types of particles show qualitatively similar RDFs. At very small radii, $g(r)$ peaks near approximately five, and it falls off gradually over a few hundred particle diameters. At lower Stokes number, the peak is slightly higher ($\gtrsim 5$), and the decrease is slower at larger radii. At higher Stokes number, the RDF appears to converge towards one at approximately 1000 particle diameters away. In either case, the peak value exceeds levels seen in turbulent channel flows (Banko, 2018) which typically had $g(r) \lesssim 2$. Still, these magnitudes are comparable to levels seen in direct numerical simulation (DNS) studies of homogeneous turbulence (Holtzer and Collins, 2016), where $g(r) \gtrsim 10$ for $St \sim 1$. The values here may be somewhat skewed because of the obvious difference in particle density inside and out of the jet core. This variation in density will change the clustering of particles.

Comparing the near-exit region (Fig. 8) and fully developed region (Fig. 9), there is a distinct difference in the RDFs. Near the exit, the peaks are similar at both Stokes numbers, and each falls off at larger radii. At first glance, the magnitudes seem very similar to the full jet region, with peak values near 5. However, we note that the RDF is higher for the larger Stokes number near the exit, suggesting that

there is more initial clustering with those high-inertia particles as they leave the pipe. At larger radial distances, the RDF curves cross, again indicating more clustering at lower Stokes number. The similarity of these two profiles could be driven by near exit effects due to the increased inertia felt by both types of particles as they leave the nozzle of the jet.

Once the mean flow is fully developed, there is a significant change in the RDF magnitudes, as observed in Fig. 9. The lower Stokes number jet has a peak that is much higher than the other regions, with $g(r) \gtrsim 11$. This suggests that these particles are more likely to cluster as the flow develops, confirming the results seen in the raw images and the Voronoï decomposition. At higher Stokes number, the magnitudes are largely unchanged from near the exit, suggesting that this flow is still developing. Even though the mean flow approaches a Gaussian velocity profile by $y/D \sim 6$, turbulent flow development can continue far beyond this axial location, even for single-phase flows (Hussein et al., 1994).

The RDF provides some useful implications for the likelihood of ash aggregation, as the collision frequency is directly proportional to $g(r)$. The peak magnitude exceeds 4 in each case, suggesting a significantly higher number of collisions within the jet flow. At the lower Stokes number, the RDF value is even higher at locations further downstream, indicating more likelihood for particle interactions. However, the collision frequency also depends on the relative velocity between particles. If all particles have similar velocities and fluctuations, as seen previously at high Stokes numbers (Shannon et al., 2023) (and Fig. 3), then they may not collide even when in close proximity (Hoffman et al., 2023).
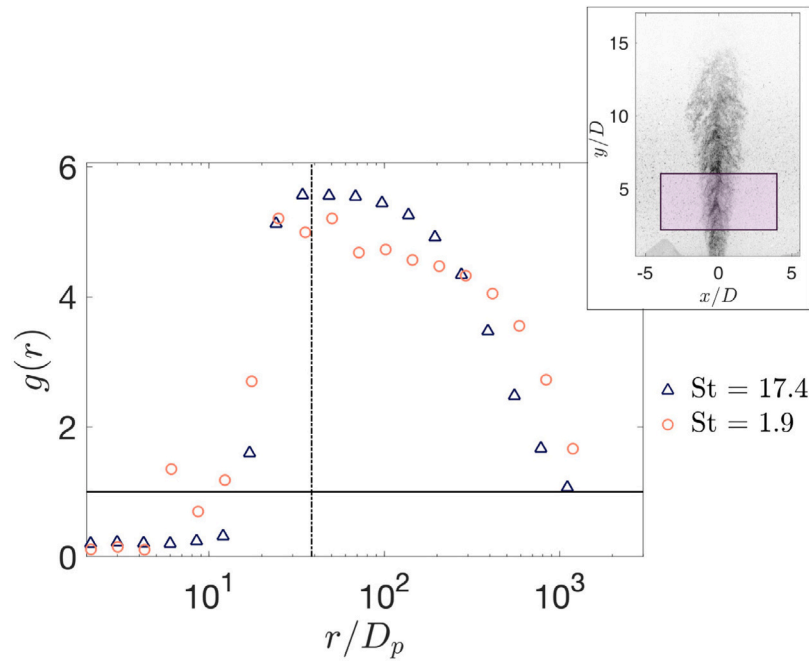
Fig. 8. Radial distribution functions, $g(r)$, for hollow glass spheres ($St = 1.9$) and nickel particles ($St = 17.4$) over the subdomain of $2 \leq y/D \leq 6$ and $-4 \leq x/D \leq 4$. The two cases are for similar Re_D and Φ of = 9600 and ~3%, respectively.
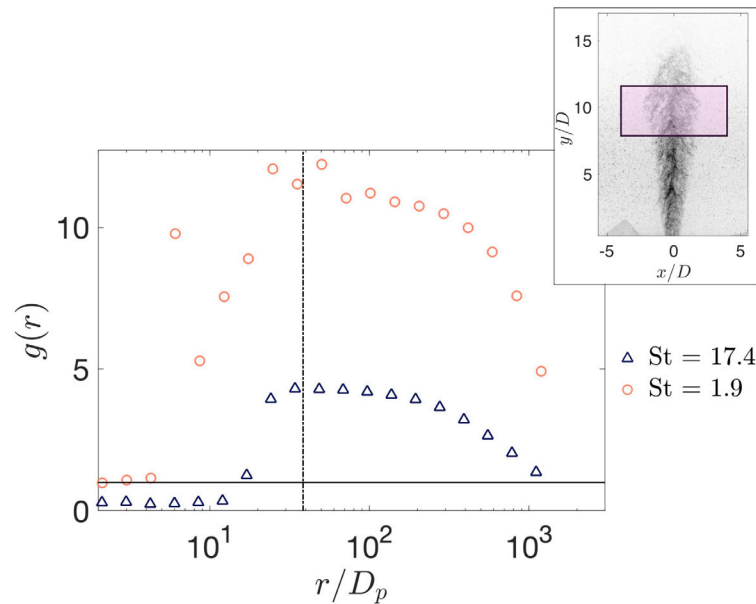

Fig. 9. Radial distribution functions, $g(r)$, for hollow glass spheres ($St = 1.9$) and nickel particles ($St = 17.4$) over the far-field region of $8 \leq y/D \leq 12$, and a transverse domain of, $-4 \leq x/D \leq 4$. Again, all cases consider $Re_D = 9600$ and $\Phi \sim 3\%$.

4.4. Computational model of aggregation

To examine the practical effects of clustering on ash aggregation, we use the Plume Model for Aggregate Prediction (PMAP), which was specifically developed to examine volcanic ash behavior (Hoffman et al., 2023). PMAP is a one-dimensional plume model, which applies control volume analysis to solve mass, momentum, and energy conservation equations. This tool is originally based on Plumeria (Mastin, 2007), which incorporates a more elaborate thermodynamic treatment of water than earlier plume models (Morton et al., 1956; Woods, 1988). Importantly, PMAP introduces conservation equations for particles, which are based on the classic Smoluchowski equation (Smoluchowski, 1918). To mitigate numerical complexity, the particles are sorted into

discrete "bins" using the fixed pivot technique (Kumar and Ramkrishna, 1996), which collects particles into groups of similar size and density.

The Smoluchowski analysis includes two semi-empirical parameters: sticking efficiency, α, and collision kernel, Γ. The former is evaluated using a micro-physical response function dependent on a collision Stokes number and water content (Hoffman and Eaton, 2023). The latter is estimated as a superposition of differential settling and turbulent mixing mechanisms:

$$\Gamma = \pi \left(r_{p,i} + r_{p,j} \right)^2 |u_{t,i} - u_{t,j}| + g\left(r\right) \sqrt{\frac{8\pi\epsilon}{15\nu}} \left(r_{p,i} + r_{p,j} \right)^3, \quad (5)$$

The first term is the product of the collision cross section for two particles with the difference between their terminal velocities. Particles
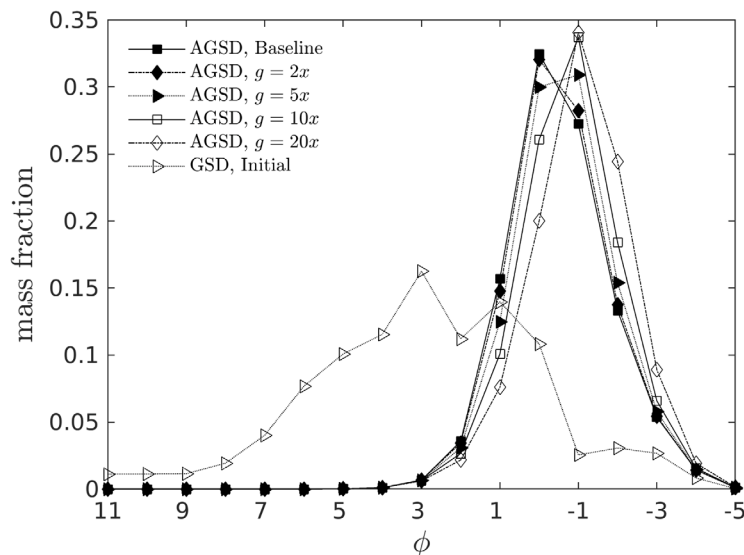
Fig. 10. Sensitivity of modeled aggregated grain size distribution to variation in the radial distribution function. ϕ is the logarithmic Krumbein scale, where larger particles have smaller values.

i and j have radii $r_{p,i}$ and $r_{p,j}$ and terminal velocities $u_{t,i}$ and $u_{t,j}$, respectively. The second term multiplies the collision cross section with a turbulent collision speed based on the Saffman–Turner limit. Notably, this also includes the effects of preferential concentration through the RDF, $g(r)$. In PMAP, the RDF is evaluated using a power law expression developed by Reade and Collins (2000) for homogeneous isotropic turbulence. For these conditions, $g \rightarrow 1$ for large particle spacings. Additional details of the PMAP tool are described by Hoffman et al. (2023).

We analyze the aggregation process for a well-characterized 23 March 2009 eruption of Redoubt Volcano in Alaska, which was used to validate PMAP earlier (Hoffman et al., 2023). In this eruption, ash aggregates fell out and froze in the surroundings, preserving the grain size distribution (GSD) before and after aggregation (Van Eaton et al., 2015). We use source conditions based on field measurements of the deposits, Doppler radar, and aggregate composition. PMAP estimates the aggregated grain size distribution (AGSD) using the particle quantities at the top of the plume, where the flow achieves neutral buoyancy. For the baseline case, this is approximately 16.8 km above sea level. To account for the effects of preferential concentration in PMAP, we rescale the RDF value, g, to larger values typical of the particle-laden jet experiments. We consider values, g/g_{base}, from 1 to 20, which encompass the full range seen in Figs. 7, 8, and 9. Although this simple rescaling does not include finer details of the turbulent particle behavior, it does provide a first-order estimate of how sensitive aggregation is to clustering effects.

Fig. 10 displays the modeled AGSD for different rescaled values of the RDF. This shows the mass fraction in various bins using the Krumbein scale, where the physical aggregate diameter, d_p, equals $2^{-\phi}$ mm. Here, $\phi = 0$ corresponds to 1 mm. We also show the initial GSD from the field measurements, which have a peak mass fraction at $\phi = 3$ (when $d_p = 125$ μm). For the baseline case, the PMAP model shows significant aggregation, with the peak mass fraction at $\phi = 0$. By increasing the RDF value by a factor of 5, there is a modest redistribution of particles to larger sizes, with nearly identical mass fractions for $\phi = 0$ and $\phi = 1$. When the RDF value increases by a factor of 20, the distribution shifts further, with the largest mass fraction at $\phi = 1$. From the Krumbein scale, this corresponds to a doubling of the

diameter at the peak. The mean grain size is estimated using the first moment of the AGSD. For the baseline case, PMAP estimates a mean size of 2.18 mm, which is more than twice as large as the initial GSD size of 0.77 mm. When the RDF is rescaled by a factor of 5, the mean grain size increases modestly to 2.34 mm. If rescaled by a factor of 20, the mean grain size rises to 2.97 mm, which would be a measurable increase in the field.

Overall, this shows that preferential concentration can have a significant influence on the resulting size distribution of aggregates. When comparing with other source parameters, this influence is similar to that of the mass eruption rate, where an increase by 100 times leads to a doubling of the peak mass fraction. However, it is not as critical as the water content, which leads to significantly larger aggregates when the water mass fraction exceeds 15% (Hoffman et al., 2023). Hence, we expect that the preferential concentration in jets would be large enough to influence the AGSD, but the mean grain size would only rise by about 50%.

To be fair, it can be complex to apply an laboratory-scale experimental study of particle clustering to full-scale plumes. Volcanic eruptions contain particle sizes ranging from microns to meters. The large scale of volcanic jets and high Reynolds numbers involved (up to 10^{10}) imply a huge range of eddy sizes between the Kolmogorov and integral length scales. Silicic eruptions such as Mount St. Helens are rich in micron-scale ash, which are likely to cluster within eddies approaching the Kolmogorov length scale (dissipation length scale). Such fine ash is also the most likely to aggregate due to other processes, such as differential settling or surface tension forces of adhered liquid water. The process of clustering within turbulent flows provides another method to drive fine ash to aggregate within volcanic plumes and ash clouds.

5. Conclusions

The clustering behavior of particles within a multiphase jet is studied through a variety of methods, examining the effects of Reynolds number, Stokes number, and mass loading. The spatial statistics of the jet show a large decrease in the fluctuations at high Stokes numbers, as observed from the cross-correlations with nickel particles. The increased inertia for these heavier, higher-Stokes number particles then

leads to a more uniform field of particle velocities within the test region. This would imply fewer collisions, even when particles are clustered.

Using Voronoï decomposition, the cell sizes clearly differ from a random Poisson distribution, though the PDFs are similar at a range of Re, St, and Φ. At a low Stokes number ($St = 1.9$), the tails of the PDF do extend to both larger and smaller cell areas, which correspond to cases where there are clear bands of particles arrayed within the shear layer vortices. The mean size of the cell area decreases when Reynolds number decreases, though this is an indication of a greater particle density rather than clustering effects. The cell area does not change significantly at increased Stokes number, but the standard deviation of the area shows high levels of clustering for when $St \sim 1$ and negligible clustering when $St \sim 17$. This indicates that the particle spacing is more uniform within the jet at higher St, without the obvious bands of particles observed at low St.

For the full spatial extent of the jet (from $2 \leq y/D \leq 12$), the radial distribution functions have a peak magnitude near 5. This is significantly higher than channel flow but comparable to homogeneous turbulence. Although channel flow is inhomogeneous, it should be noted that it is a fully developed flow field whereas, in these jet flows, flow is developing throughout. Furthermore, the dispersion of the jet plays a large role in the locations and magnitudes of the clustering. At high Stokes number, the peak RDF magnitude is similar in both the near exit and downstream regions, implying slower development. At low Stokes number, the peak is significantly higher downstream, with the radial distribution function $g \sim 11$, implying more likelihood of collisions due to the clustering. Based on computational aggregation models, this can increase the peak aggregate diameter by a factor of two.

Overall, we find that all cases present some levels of clustering compared to a random distribution of particles, though it is minimal for the high Stokes numbers and the highest Reynolds number. Hollow glass particles (at low St) at lower Reynolds numbers had higher standard deviation for the mean area of the Voronoï cells, indicating the greatest amount of clustering. Farther downstream, the magnitude of the RDF is significantly higher at low St, corresponding to higher collision frequencies in the fully developed jet.

CRediT authorship contribution statement

Bianca Viggiano: Formal analysis, Investigation, Writing – original draft, Writing – review & editing. **Kris Gish:** Formal analysis, Investigation. **Stephen Solovitz:** Conceptualization, Data curation, Formal analysis, Funding acquisition, Investigation, Methodology, Supervision, Writing – original draft, Writing – review & editing. **Raúl Bayoán Cal:** Conceptualization, Funding acquisition, Methodology, Supervision, Writing – review & editing, Investigation, Writing – original draft.

Declaration of competing interest

The authors declare that they have no known competing financial interests or personal relationships that could have appeared to influence the work reported in this paper.

Data availability

PIV data are available through: Solovitz, S. (2022). Particle-laden jet PIV data [Dataset]. Harvard Dataverse. https://doi.org/10.7910/DVN/HDBMHV. All data can be made available upon request.

Acknowledgments

References

Baker, L., Frankel, A., Mani, A., Coletti, F., 2017. Coherent clusters of inertial particles in homogeneous turbulence. J. Fluid Mech. 833, 364–398.

Balachandar, S., Eaton, J.K., 2010. Turbulent dispersed multiphase flow. Annu. Rev. Fluid Mech. 42, 111–133.

Banko, A.J., 2018. Radiation Absorption by Inertial Particles in a Turbulent Square Duct Flow (Ph.D. thesis). Stanford University.

Basset, T., Viggiano, B., Barois, T., Gibert, M., Mordant, N., Cal, R., Volk, R., Bourgoin, M., 2022. Entrainment, diffusion and effective compressibility in a self-similar turbulent jet. J. Fluid Mech. 947, A29.

Beckett, F., Rossi, E., Devenish, B., Witham, C., Bonadonna, C., 2022. Modelling the size distribution of aggregated volcanic ash and implications for operational atmospheric dispersion modelling. Atmos. Chem. Phys. 22 (5), 3409–3431.

Bell, J.H., Mehta, R.D., 1988. Contraction Design for Small Low-Speed Wind Tunnels. Tech. Rep..

Birzer, C.H., Kait, P.A.M., Nathan, G.J., 2011. A method to provide statistical measures of large-scale instantaneous particle clusters from planar images. Exp. Fluids 51, 641–656.

Capone, A., Moscato, G., Romano, G., 2023. Role of density ratio on particle dispersion in a turbulent jet. Phys. Fluids 35 (1).

Chen, L., Goto, S., Vassilicos, J.C., 2006. Turbulent clustering of stagnation points and inertial particles. J. Fluid Mech. 553, 143–154.

Chen, S., Li, S., Marshall, J.S., 2019. Exponential scaling in early-stage agglomeration of adhesive particles in turbulence. Phys. Rev. Fluids 4 (2), 024304.

Costa, A., Folch, A., Macedonio, G., 2010. A model for wet aggregation of ash particles in volcanic plumes and clouds: 1. Theoretical formulation. J. Geophys. Res. 115 (B9), B09201.

Dunn, M.G., 2012. Operation of gas turbine engines in an environment contaminated with volcanic ash. J. Turbomach. 134 (5).

Eaton, J.K., Fessler, J.R., 1994. Preferential concentration of particles by turbulence. Int. J. Multiph. Flow 20 (S1), 169–209.

Edelsbrunner, H., Seidel, R., 1986. Voronoi diagrams and arrangements. Discrete Comput. Geom. 1 (1), 25–44.

Egan, S.D., Stuefer, M., Webley, P.W., Lopez, T., Cahill, C.F., Hirtl, M., 2020. Modeling volcanic ash aggregation processes and related impacts on the April–May 2010 eruptions of Eyjafjallajökull volcano with WRF-Chem. Nat. Hazards Earth Syst. Sci. 20 (10), 2721–2737.

Elgobashi, S., Truesdell, G.C., 1992. Direct simulation of particle dispersion in a decaying isotropic turbulence. J. Fluid Mech. 242, 655–700.

Esmaily, M., Villafane, L., Banko, A.J., Iaccarino, G., Eaton, J.K., Mani, A., 2020. A benchmark for particle-laden turbulent duct flow: A joint computational and experimental study. Int. J. Multiph. Flow 132, 103410.

Ferenc, J.-S., Néda, Z., 2007. On the size distribution of Poisson Voronoi cells. Physica A 385 (2), 518–526.

Fessler, J.R., Kulick, J.D., Eaton, J.K., 1994. Preferential concentration of heavy particles in a turbulent channel flow. Phys. Fluids 6 (11), 3742–3749.

Folch, A., Costa, A., Durant, A., Macedonio, G., 2010. A model for wet aggregation of ash particles in volcanic plumes and clouds: 2. Model application. J. Geophys. Res. 115 (B9), B09202.

Gilbert, J.S., Lane, S.J., 1994. The origin of accretionary lapilli. Bull. Volcanol. 56 (5), 398–411.

Gualtieri, P., Picano, F., Sardina, G., Casciola, C.M., 2013. Clustering and turbulence modulation in particle-laden shear flows. J. Fluid Mech. 715, 134–162.

Han, D., 2001. Study of Turbulent Nonpremixed Jet Flames Using Simultaneous Measurements of Velocity and CH Distribution (Ph.D. thesis). Stanford University.

Hoffman, D.W., Eaton, J.K., 2023. Experimental investigation of particle aggregation in a humid and turbulent environment. Int. J. Multiph. Flow 163, 104423.

Hoffman, D.W., Mastin, L.G., Van Eaton, A.R., Solovitz, S.A., Cal, R., Eaton, J.K., 2023. A one-dimensional volcanic plume model for predicting ash aggregation. J. Geophys. Res.: Solid Earth e2023JB027002.

Holtzer, G.L., Collins, L.R., 2002. Relationship between the intrinsic radial distribution function for an isotropic field of particles and lower-dimensional measurements. J. Fluid Mech. 459, 93–102.

Holtzer, G.L., Collins, L.R., 2016. The effect of Reynolds number on inertial particle dynamics in isotropic turbulence. Part 1. Simulations without gravitational effects. J. Fluid Mech. 796, 617–658.

Hussein, H.J., Capp, S.P., George, W.K., 1994. Velocity measurements in a high-Reynolds-number, momentum-conserving, axisymmetric, turbulent jet. J. Fluid Mech. 258, 31–75.

Kays, W.M., Crawford, M.E., 1993. Convective Heat and Mass Transfer, second ed. McGraw-Hill, New York.

Kulick, J.D., Fessler, J.R., Eaton, J.K., 1994. Particle response and turbulence modification in fully developed channel flow. J. Fluid Mech. 277, 109–134.

Kumar, S., Ramkrishna, D., 1996. On the solution of population balance equations by discretization–I. A fixed pivot technique. Chem. Eng. Sci. 51, 1311–1332.

Landau, L., Lifshitz, E., 1980. Statistical Physics. Butterworth Heinemann, Oxford, UK.

Larsen, M.L., Shaw, R.A., 2018. A method for computing the three-dimensional radial distribution function of cloud particles from holographic images. Atmos. Meas. Tech. 11 (7), 4261–4272.

Lau, T.C.W., Frank, J.H., Nathan, G.J., 2019. Resolving the three-dimensional structure of particles that are aerodynamically clustered by a turbulent flow. Phys. Fluids 31, 071702.

Lau, T.C.W., Nathan, G.J., 2017. A method for identifying and characterising particle clusters in a two-phase turbulent jet. Int. J. Multiph. Flow 88, 191–204.

Longmire, E.K., Eaton, J.K., 1992. Structure of a particle-laden round jet. J. Fluid Mech. 236, 217–257.

Mastin, L.G., 2007. A user-friendly one-dimensional model for wet volcanic plumes. Geochem. Geophys. Geosyst. 8 (3).

Monchaux, R., Bourgoin, M., Cartellier, A., 2010. Preferential concentration of heavy particles: A Voronoï analysisResolving the three-dimensional structure of particles that are aerodynamically clustered by a turbulent flow. Phys. Fluids 22, 103304.

Monchaux, R., Bourgoin, M., Cartellier, A., 2012. Analyzing preferential concentration and clustering of inertial particles in turbulence. Int. J. Multiph. Flow 40, 1–18.

Morton, B.R., Taylor, G., Turner, J.S., 1956. Turbulent gravitational convection from maintained and instantaneous sources. Proc. R. Soc. Lond. A: Math. Phys. Eng. Sci. 234 (1196), 1–23.

Nilsen, C., Andersson, H.I., Zhao, L., 2013. A Voronoï analysis of preferential concentration in a vertical channel flow. Phys. Fluids 25 (11).

Obligado, M., Teitelbaum, T., Cartellier, A., Mininni, P., Bourgoin, M., 2014. Preferential concentration of heavy particles in turbulence. J. Turbul. 15 (5), 293–310.

Raffel, M., Willert, C.E., Kompenhans, J., 2013. Particle Image Velocimetry: A Practical Guide. Springer.

Reade, W.C., Collins, L.R., 2000. Effect of preferential concentration on turbulent collision rates. Phys. Fluids 12 (10), 2530–2540.

Saffaraval, F., Solovitz, S.A., 2012. Near-exit flow physics of a moderately overpressured jet. Phys. Fluids 24 (8), 086101.

Saffman, P.G., Turner, J.S., 1956. On the collision of drops in turbulent clouds. J. Fluid Mech. 1 (1), 16–30.

Schumacher, R., 1994. A reappraisal of Mount St. Helens' ash clusters–depositional model from experimental observation. J. Volcanol. Geotherm. Res. 59, 253–260.

Shannon, L.K., Viggiano, B., Cal, R.B., Mastin, L.G., Van Eaton, A.R., Solovitz, S.A., 2023. Flow development and entrainment in turbulent particle-laden jets. J. Geophys. Res.: Atmos. e2022JD038108.

Smoluchowski, M., 1918. Versuch einer mathematischen Theorie der Koagulationskinetic kolloider Lösungen. Z. Phys. Chem. 92, 128–168.

Solovitz, S.A., Mastin, L.G., Saffaraval, F., 2011. Experimental study of near-field entrainment of moderately overpressured jets. J. Fluids Eng. 133 (5), 051304.

Sorem, R.K., 1982. Volcanic ash clusters: Tephra rafts and scavengers. J. Volcanol. Geotherm. Res. 13 (1), 63–71.

Sparks, R.S.J., Bursik, M.I., Carey, S.N., Gilbert, J.S., Glaze, L.S., Sigurdsson, H., Woods, A.W., 1997. Volcanic Plumes. John Wiley, Chichester, UK.

Squires, K.D., Eaton, J.K., 1990. Particle response and turbulence modification in isotropic turbulence. Phys. Fluids A 2 (7), 1191–1203.

Sumbekova, S., Cartellier, A., Aliseda, A., Bourgoin, M., 2017. Preferential concentration of inertial sub-Kolmogorov particles: the roles of mass loading of particles, Stokes numbers, and Reynolds numbers. Phys. Rev. Fluids 2 (2), 024302.

Sundaram, S., Collins, L.R., 1997. Collision statistics in an isotropic particle-laden turbulent suspension. Part 1. Direct numerical simulations. J. Fluid Mech. 335, 75–109.

Tagawa, Y., Mercado, J.M., Prakash, V.N., Calzavarini, E., Sun, C., Lohse, D., 2012. Three-dimensional Lagrangian Voronoï analysis for clustering of particles and bubbles in turbulence. J. Fluid Mech. 693, 201–215.

Telling, J., Dufek, J., Shaikh, A., 2013. Ash aggregation in explosive volcanic eruptions. Geophys. Res. Lett. 40, 2355–2360.

Tomita, K., Kanai, T., Kobayaski, T., Oba, N., 1985. Accretionary lapilli formed by the eruption of Sakurajima volcano. J. Jpn. Assoc. Mineral. Petrol. Econ. Geol. 80, 49–54.

Van Eaton, A.R., Mastin, L.G., Herzog, M., Schwaiger, H.F., Schneider, D.J., Wallace, K.L., Clarke, A.B., 2015. Hail formation triggers rapid ash aggregation in volcanic plumes. Nature Commun. 6, 7860.

Viggiano, B., Basset, T., Solovitz, S., Barois, T., Gibert, M., Mordant, N., Chevillard, L., Volk, R., Bourgoin, M., Cal, R., 2021a. Lagrangian diffusion properties of a free shear turbulent jet. J. Fluid Mech. 918, A25.

Viggiano, B., Sakradse, G., Smith, S., Mungin, R., Ramasubramanian, P., Ringle, D., Travis, K., Ali, N., Solovitz, S., Cal, R.B., 2021b. Intermittent event evaluation through a multifractal approach for variable density jets. Chaos, Solitons & Fractals 146, 110799.

Wicker, R.B., Eaton, J.K., 2001. Structure of a swirling, recirculating coaxial free jet and its effect on particle motion. Int. J. Multiph. Flow 27 (6), 949–970.

Wilson, T.M., Jenkins, S., Stewart, C., 2015. Impacts from volcanic ash fall. In: Volcanic Hazards, Risks and Disasters. Elsevier, Amsterdam.

Woods, A.W., 1988. The fluid dynamics and thermodynamics of eruption columns. Bull. Volcanol. 50 (3), 169–193.

Zhang, R., Yang, Z., Detwiler, R., Li, D., Ma, G., Hu, R., Chen, Y.-F., 2023. Liquid cohesion induced particle agglomeration enhances clogging in rock fractures. Geophys. Res. Lett. 50 (5), e2022GL102097.